Nanoscale

PAPER

View Article Online
View Journal | View Issue

Cite this: *Nanoscale*, 2021, **13**, 1652

Exfoliation of boron carbide into ultrathin nanosheets†

Yuqi Guo,[a] Adway Gupta,[b] Matthew S. Gilliam,[c,d] Abhishek Debnath,[c,d] Ahmed Yousaf,[c,d] Sanchari Saha,[c,d] Mark D. Levin,[a] Alexander A. Green, *[c,d,e] Arunima K. Singh *[b] and Qing Hua Wang *[a]

Liquid phase exfoliation (LPE) is a method that can be used to produce bulk quantities of two-dimensional (2D) nanosheets from layered van der Waals (vdW) materials. In recent years, LPE has been applied to several non-vdW materials with anisotropic bonding to produce nanosheets and platelets, but it has not been demonstrated for materials with strong isotropic bonding. In this paper, we demonstrate the exfoliation of boron carbide (B_4C), the third hardest known material, into ultrathin nanosheets. B_4C has a structure consisting of strongly bonded boron icosahedra and carbon chains, but does not have anisotropic cleavage energies to suggest that it can be readily cleaved into nanosheets. B_4C has been widely studied for its very high melting point, high mechanical strength, and chemical stability, as well as its zero- and one-dimensional nanostructured forms. Herein, ultrathin nanosheets are successfully prepared by sonication of B_4C powder in organic solvents and are characterized by microscopy and spectroscopy. Density functional theory (DFT) simulations reveal that B_4C can be cleaved along several different crystallographic planes with similar energetic favourability, facilititated by an unexpected mechanism of breaking boron icosahedra and forming new boron-rich cage structures at the surface. Atomic force microscopy (AFM) shows that the nanosheets produced by LPE are as thin as 5 nm, with an average thickness of 31.4 nm and average area of 16 000 nm^2. Raman spectroscopy shows that many of the nanosheets exhibit additional carbon-rich peaks that change with laser irradiation, which are attributed to atomic rearrangements and amorphization at the nanosheet surfaces, consistent with the diverse cleavage planes. High-resolution transmission electron microscopy (HRTEM) demonstrates that many different cleavage planes exist among the exfoliated nanosheets, in agreement with DFT simulations. This work elucidates the exfoliation mechanism of 2D B_4C and suggests that LPE can be applied to generate nanosheets from a variety of non-layered and non-vdW materials.

Received 8th November 2020,
Accepted 31st December 2020

DOI: 10.1039/d0nr07971e

rsc.li/nanoscale

Introduction

Liquid-phase exfoliation (LPE) is a method to produce a large number of mono- or few-layer nanomaterials by exfoliating bulk materials with a layered structure, thus producing two-dimensional (2D) nanosheets with nanometre-scale thickness but much larger lateral dimensions.[1–4] Most 2D nanosheets produced by LPE have come from bulk layered solids with strong in-plane bonding and weaker van der Waals (vdW) interplanar bonds. Thus, traditional exfoliated vdW materials include graphene, boron nitride (h-BN), transition metal dichalcogenides (TMDs), oxides (Ti oxides, Mn oxides, *etc.*), MoO_2 and layered double hydroxides (LDHs).[1,5–8]

In the past few years, layered but non-vdW materials have been exfoliated into 2D nanosheets. Layered MgB_2, one of the metal diboride (MB_2) family, was used to produce nano-accordions and nanosheets by Das *et al.* utilizing liquid exfoliation in water.[9] In their work, the few layer-thick MgB_2 nanosheets become oxidized but act as a good candidate for flame retardant and mechanical strengthening applications.[9] The metal diborides have a more complex bonding environment than vdW layered materials due to the ionic character of metal–boron interactions. We have also recently demonstrated the LPE production of metal diboride nanosheets of eight different compositions by dispersing them in organic sol-

[a]*Materials Science and Engineering, School for Engineering of Matter, Transport and Energy, Arizona State University, Tempe, Arizona 85287, USA. E-mail: qhwang@asu.edu*
[b]*Department of Physics, Arizona State University, Tempe, Arizona 85287, USA. E-mail: arunimasingh@asu.edu*
[c]*Biodesign Center for Molecular Design and Biomimetics, The Biodesign Institute, Arizona State University, Tempe, Arizona 85287, USA. E-mail: aagreen@bu.edu*
[d]*School of Molecular Sciences, Arizona State University, Tempe, Arizona 85287, USA*
[e]*Department of Biomedical Engineering, Boston University, Boston, MA 02215, USA*
†Electronic supplementary information (ESI) available: Additional Raman and computational results. See DOI: 10.1039/d0nr07971e

vents.[10] Furthermore, Puthirath Balan *et al.* have recently shown the exfoliation of atomically thin sheets from the non-vdW crystals Fe_2O_3 (hematite), and $FeTiO_3$ (ilmenite).[11,12] The two-dimensional "hematene" and "ilmenene" sheets in those earlier works were shown to enhance the visible photocatalytic activity of TiO_2 nanotubes.

However, these earlier works with non-vdW crystals still start with layered materials. Backes *et al.* recently showed that the aspect ratio (length : thickness) of liquid-exfoliated nanosheets are controlled by the ratio between the in-plane-tearing energy and the out-of-plane-peeling energy, so that layered materials with large mechanical anisotropy tend to yield nanosheets with large aspect ratios.[13] This analysis also implies that non-layered materials with anisotropic bonding schemes can also be exfoliated into non-layered quasi-2D materials.[14,15] Hence the production of nanosheets and nanoplatelets from the exfoliation of non-layered materials could notably expand the 2D material family, building on the exfoliation of non-layered materials such as Fe_2O_3, WO_3, Se, Te, pyrite and metal oxides.[11,14,16–18]

Boron carbide has been studied broadly in the past decades, and it is the third hardest known material surpassed only by diamond and boron nitride.[19,20] The two main recognized crystal structures of B_4C are B_{12} icosahedra with C–C–C chains and $B_{11}C$ icosahedra with C–B–C chains.[21–23] The latter structure is more strongly supported based on the recent studies of improved X-ray and neutron diffraction, and nuclear magnetic resonance.[19,24–28] Theoretical calculations and vibrational spectra also confirmed that the $B_{11}C$ icosahedra with the carbon atom at the polar site is energetically more favourable.[21,29–31] The crystal structure of B_4C with the $B_{11}C$ icosahedra and C–B–C chains is shown in Fig. 1.

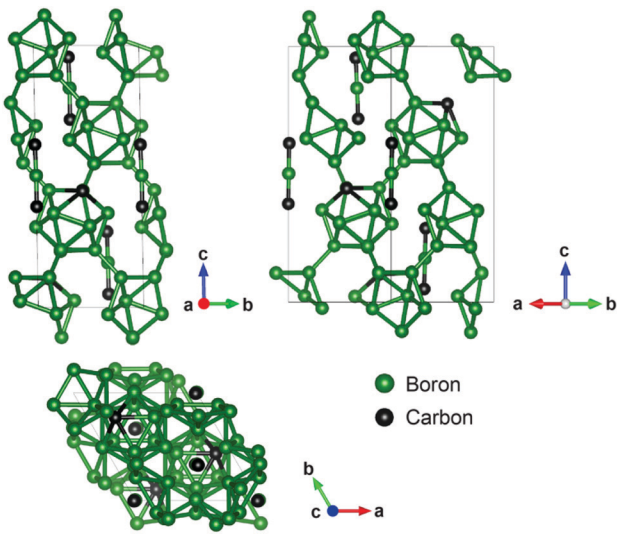

Fig. 1 Crystal structure of boron carbide (B_4C). The structure of B_4C consists of 12-atom icosahedra and 3-atom chains. The form of the structure with $B_{11}C$ icosahedra and C–B–C chains is presented here. The unit cells along three different directions are illustrated.

Boron carbide is also known for its exceptional chemical stability and good electronic conductivity, which makes it suitable for making fuel cells and batteries.[32–35] Its high melting point (2763 °C), high strength and the high content of ^{10}B isotope also makes B_4C widely used in wear-resistant applications and neutron absorbing composites.[36–38] B_4C has also been shown to have enhanced mechanical properties in metal composites, and has been incorporated into hybrid structures.[39–41] Thus, the production of two-dimensional B_4C has significant potential for expanding its processing and applications.

B_4C has been previously studied in its zero-dimensional (0D) and one-dimensional (1D) forms.[42–44] For example, Mortensen *et al.* showed how B_4C nanoparticles can be used in T cell-guided boron neutron capture therapy.[45] Guan *et al.* also synthesized B_4C nanowires and showed their thermal properties are diameter-dependent.[46]

Although the synthesis of B_4C 2D nanosheets has been reported elsewhere with thickness ranging from 10 to 100 nm, the synthesis method required high temperature chemical reactions (1450 to 1950 °C) or other complex synthesis methods.[47–49] Recently, Qiu *et al.* formed B_4C nanosheets by stripping bulk B_4C in an ultrasonic cell disruptor, and found that they could act as electrocatalysts toward N_2-fixation in hydrochloric acid.[50,51] However, this work provided no detailed characterization or discussion of the thickness and the properties of the nanosheets, and the mechanism behind the production of the B_4C nanosheets was not explained. So to the best of our knowledge, there have been no previous studies that both demonstrate the liquid-phase exfoliation of B_4C nanosheets from bulk powder and also their characterization in terms of morphology, size, thickness metrics, and the mechanism behind the exfoliation of this non-vdW material into 2D or quasi-2D structures.

In this study, we produce B_4C nanosheets by a mild processing method of tip sonicating B_4C bulk powder in several different organic solvents and confirm the nanosheet structures by atomic force microscopy (AFM) and transmission electron microscopy (TEM). We chose four planes according to an initial observation of the B_4C crystal structure that suggested more favourable cleavage (*i.e.* no cuts through icosahedra) and modelled them using density functional theory (DFT). Our computational results showed the corresponding exfoliation energy for four selected exfoliated planes (001), (012), (101) and (300) have binding energies of 0.056, 0.105, 0.116 and 0.113 eV per atom, respectively, which are all below the thermodynamic stability threshold energy of 0.2 eV per atom for a free-standing single-layer or few-layer nanosheet.[52,53] The evolution of B_4C Raman spectra with increasing laser irradiation time revealed four types of B_4C flakes in terms of the changing intensities of various peaks, which could be due to the combination of B_4C amorphization and exfoliation of different planes. Histograms of the B_4C thickness and area distributions provided evidence for substantial production of thin B_4C nanosheets. The successful mass production of B_4C

nanosheets is promising for applications such as mechanical strengthening and catalysis.

Methods

Computational modelling

We studied the energy of exfoliation of B_4C along several high-symmetry planes using first-principles simulations. All simulations are based on DFT using the projector-augmented wave (PAW) method as implemented in the plane-wave code VASP.[54–57] The simulations were performed using the vdW-DF-optB88 exchange–correlation functional, that provides an excellent description of the non-local vdW interactions in materials.[58–60] A *k*-point density of 40 $Å^{-1}$ with a 600 eV energy cut-off results in an accuracy of the total energies of 5 meV per atom. The structures are relaxed until the forces on the atoms are less than 0.005 eV $Å^{-1}$. The simulations of B_4C with cleavage along the different planes and different surface terminations were performed in a slab geometry with minimum slab thickness of 15 Å and a minimum vacuum spacing of 15 Å. To eliminate effects from surface dipoles, symmetric slabs were used. Slabs were generated by the pymatgen package.[61]

Since the different simulated slabs have different numbers of atoms, we need to normalise the energy of the structures to draw conclusions about their relative stability. We define the formation energy of slabs as

$$\Delta E_f = \frac{\left(E_{slab} - N^C_{slab}\frac{E_{Graphite}}{N^C_{Graphite}} - N^B_{slab}\frac{E_{\alpha\text{-Boron}}}{N^B_{\alpha\text{-Boron}}}\right)}{N_{slab}} \quad (1)$$

where E_{slab}, $E_{Graphite}$, and $E_{\alpha\text{-Boron}}$ are the energies of the slab, bulk graphite, and bulk α-boron, respectively. $N^C_{Graphite}$ and $N^B_{\alpha-Boron}$ are the number of atoms of carbon and boron in their respective bulk structures; and N_{slab}, N^C_{Slab}, and N^B_{Slab} are the number of total atoms, carbon atoms and boron atoms in the slab, respectively. For the bulk counterpart of carbon, we chose graphite in the *Cmme* space group (Materials Project ID mp-568286).[62] For the bulk counterpart of boron, we use the ground state structure of boron, α-boron, in the space group $R\bar{3}m$ (Materials Project ID mp-160). Since the structure of α-boron is very similar to that of B_4C with similar boron icosahedra at the corners of the unit cell, it was a suitable choice for the bulk boron.

Exfoliation of boron carbide nanosheets

Boron carbide nanosheets were obtained by LPE as follows: 0.4 g of B_4C powder (Sigma, 378119) was mixed with 6 mL of organic solvent in 15 mL polypropylene tubes or 7 mL glass vials, and then the mixture was subjected to tip ultrasonication at 20% amplitude (Branson Digital Sonifier 450D, 3 mm diameter tip) for one hour. The solvents used were isopropanol (IPA, Sigma, I9030), acetone (ACT, VWR, BDH110), 1-methyl-2-pyrrolidinone (NMP, Sigma, 270458), *N*,*N*-dimethylformamide (DMF, Sigma, 227056), and *N*,*N*-dimethylacetamide (DMAc, Sigma, D137510). The sonicated mixture was then centrifuged for 5 minutes at 5000 RCF and the supernatant dispersion of B_4C nanosheets was collected and used for characterization.

For the mechanical exfoliation (ME) of boron carbide, Si wafers with 300 nm SiO_2 (Wafernet, Inc.) were coated a 20 nm Ti adhesion layer and 200 nm of Au using physical vapor deposition (PVD) to increase adhesion with the B_4C material. The coated wafers were cleaned in ultrasonic baths of acetone and isopropanol for 5 minutes each sequentially, and then blown dry by ultrahigh purity nitrogen gas. The substrates were placed on a hot plate at 120 °C. The bulk boron carbide powder was exfoliated on adhesive scotch tape and pressed onto the heated substrates and peeled away. The deposited samples on substrates were annealed in vacuum at 300 °C for 5 hours with 200 sccm Ar flow to remove tape residue and other contamination from the ambient environment.

Raman spectroscopy

Raman spectroscopy was conducted using a WITec alpha300R confocal Raman microscope system. The laser excitation wavelength was 532 nm, the objective lens was 100× with ~1 μm diameter laser spot size. The total laser power was kept at 20 mW (2.547 MW cm^{-2}) to improve the signal-to-noise ratio, and the 600 grooves per mm grating was used. For Raman spectrum evolution analysis, the Raman spectrum was continuously taken every 30 seconds until no changes were observed in the intensity of all the peaks over the last 60 seconds.

Atomic force microscopy (AFM)

Atomic force microscopy (AFM) imaging was performed in ScanAsyst non-contact mode on a Bruker Multimode V system with ScanAsyst-Air tips (Bruker, tip diameter 2 nm). The images were processed by the Gwyddion software package version 2.52.[63]

Statistical analysis of B_4C nanosheet thickness and area

Thickness and area distributions of B_4C nanosheets were measured by AFM. Sapphire substrates (1 cm × 1 cm) were sonicated in acetone and then in IPA for 5 min each to clean them. The B_4C/IPA dispersion from LPE was spin coated (static spin coating) for 1 min on the cleaned sapphire substrate three times at a speed of 2500 rpm. The sapphire substrate was then annealed in a tube furnace at 500 °C with Ar flowing (200 sccm flow rate) for 3 h to remove contamination. AFM imaging was used to measure the morphology and height profiles of annealed B_4C nanosheets. Histograms of nanosheet thickness and area for LPE-produced nanosheets were plotted by first processing all AFM images in Gwyddion[34] to achieve clear contrast and proper image flattening. Height profiles were then obtained on flakes with clean and sharp boundaries. ImageJ was used to obtain the area for each flake used in the area statistics. In total, 169 flakes were counted based on six AFM images. Then Matlab R2017a was used to plot the histograms.

Transmission electron microscopy (TEM) and high-resolution TEM (HRTEM)

The B_4C nanosheet samples were prepared by liquid-phase exfoliation as described above. The dispersions were then dropped onto lacey carbon-coated 400 mesh Cu TEM grids (Pacific Grid Tech) and dried before imaging. Philips CM-12 (80 kV accelerating voltage) and FEI Titan (300 kV accelerating voltage) were used for TEM and HRTEM imaging, respectively.

The Gatan Microscopy Suite (GMS) software was used to analyse the HRTEM images and their corresponding fast Fourier transforms (FFTs). The powder X-ray diffraction data contained within PDF Card 00-035-0798 and lattice spacings we obtained from the FFTs were used to assign the Miller indices to the planes observed in the HRTEM images.

The Miller indices of proposed exfoliation planes were calculated using a cross product calculation between observed crystal planes indexed *via* the FFTs of the HRTEM images. A generalized cross product is defined as follows:

$$A_3 = A_1 \times A_2 \quad (2)$$

where A_3 represents the proposed exfoliation plane with Miller indices $(h_3k_3l_3)$, while A_1 and A_2 observed planes perpendicular to the proposed exfoliation plane, with Miller indices $(h_1k_1l_1)$ and $(h_2k_2l_2)$ respectively. The Miller indices of A_1 and A_2 were assigned based on the observed d-spacings from the FFTs generated from the HRTEM images. We assumed that the flakes being investigated were flat on the TEM grids, and that the planes where the d-spacings were obtained were aligned parallel to the electron beam.

Results and discussion

Computations of B_4C cleavage planes

Formation energies. We used DFT to compute the formation energies of different slabs of B_4C using eqn (1) as described in the computational methods section for cleavage along four different planes: (300), (001), (101) and (012). We chose these particular planes according to the symmetry in the crystals. The (300) and (001) planes cleave the bulk B_4C parallel and perpendicular to the direction of the C–C–C chains, respectively. The other two planes, (101) and (012), have an arbitrary oblique angle with the C–C–C chains. The comparison of the energies for these planes of cleavage can help us ascertain if there is a correlation between the stability of the 2D slabs and the angle they make with the C–C–C chains.

While the majority of the experimental results in this work are discussed in the context of a B_4C structure with C–B–C chains, we pursue our computations with C–C–C chains for two reasons. First, structures with the C–B–C chain are computationally expensive to simulate, with more than 50 possible surface terminations for the chosen planes each containing 90 to 225 atoms. In comparison, only 29 terminations are needed to simulate the B_4C slabs with C–C–C chains, with each containing 46 to 176 atoms. Second, upon simulating the bulk structures and some slabs, we noticed that the structures with C–B–C chains follow the same energy trends as that of the C–C–C chains, both for the bulk and for similar terminations in the slabs. For the bulk, the total energy for the structure with C–B–C chains is lower than the one with C–C–C chains by 0.075 eV per atom. In the (001) slab, for terminations 2 and 6 (defined in Fig. 2), the slabs with C–B–C bonds have formation energies lower than the ones with C–C–C bonds by 0.042 eV per atom and 0.071 eV per atom respectively.

The formation energies of the different terminations along these directions is shown in Fig. 2. In each panel, different terminations at slightly shifted positions are indicated by the horizontal lines labelled t1, t2, *etc*. The formation energies ΔE_f are plotted in the bar graphs for each termination in each plane. The minimum ΔE_f for the planes (300) and (001) are 0.113 and 0.056 eV per atom, respectively, while that for the planes (101) and (012) are 0.116 and 0.105 eV per atom, respectively. Interestingly, these energies being quite close to each other suggest that there is not a significant preference in the choice of a particular cleavage plane. Also, as the structures

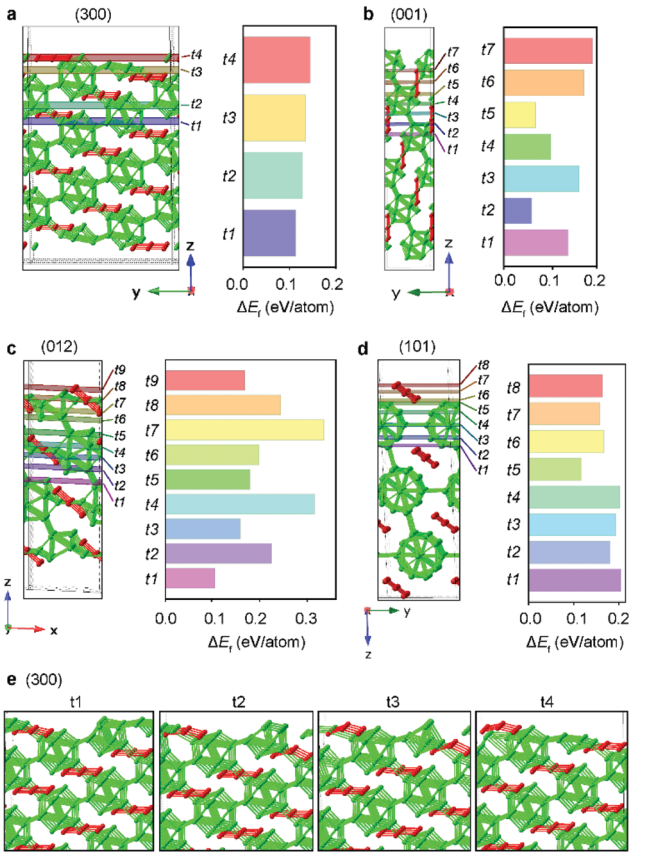

Fig. 2 Energies of cleavage planes. The figures show the formation energies of different terminations for the cleavage along the different planes of B_4C: (a) (300), (b) (001), (c) (012) and (d) (101). Boron atoms are green while carbon atoms are red. The different terminations for each cleavage plane are numbered tn, where n is counted up from bottom to top. (e) Relaxed structures for different terminations for cleavage along the (300) plane.

with C–C–C bonds all have formation energies below the threshold of 0.2 eV per atom for free-standing monolayer or few-layer nanosheets, we can conclude so will the structures with C–B–C bonds.[52,53] Thus, these results suggest that it is favourable to form B_4C nanosheets along many possible directions or planes.

Relaxed structures. The reason behind the hardness of bulk B_4C, and in fact any structure composed of boron icosahedra, is a unique covalent bonding scheme called three-centre bonding.[64] Boron is a trivalent atom and can thus contribute at most three electrons to form covalent bonds. However, in a B_{12} icosahedron, each B atom has five neighbouring B atoms. Clearly, this cannot be attributed to regular two-centre bonding. The resolution is that each triplet of B molecules, which comprise a face of the icosahedron, share a pair of electrons between them. This results in a peak in the electron density within the triangular faces of the icosahedra. This three-centre bonding makes the B icosahedra particularly stable and hard structures. In addition, the bonds between the icosahedra are just as strong, if not stronger than the bonding within the icosahedra, resulting in B_4C having extremely favourable physical and thermoelectric properties.[65,66]

As a result, we might expect that the structures will be easier to cleave along the covalently bonded linear C–C–C chains such that the B icosahedra remain intact. However, from our simulations, we conclude that this is not the case. Bader charge analysis shows that C–C–C and C–B–C chains are more ionic than the B–B bonds, making them much harder to cleave.[67] According to Bader charge analysis, B sites in the B_4C structure C–C–C (C–B–C) chains have an average of −0.51 (−0.17) electrons and C sites 2.03 (0.69).

Thus, we might expect that any termination that cleaves through the B-icosahedra will be energetically expensive as the system will transition from an exceptionally stable structure to a seemingly unstable one. Again, we see from our computational results that this is not true. Any termination that has broken B-icosahedra, after relaxation rearranges into new, stable cages with fewer than 12 B atoms. Fig. 2e shows the relaxed structure for the different terminations for cleavage along the (300) plane. All the other relaxed structures for the different cleavage planes and different terminations for each plane can be found in the ESI (Fig. S1–S3†) in images that show the formation of new, smaller B structures at the surfaces of the slabs. These structures are composed of a combination of three-centre and regular two-centre covalent bonds depending on the number of B atoms in the structure. The energy required to break the icosahedra is thus compensated for by the formation of these smaller B structures.

Liquid-phase exfoliation of B_4C

Following the unexpected computational results showing that cleavage along different planes is energetically favourable and breakage of the stable B icosahedra in favour of forming new smaller B cages, we used experimental methods to cleave B_4C. Few-layer B_4C nanosheets were prepared by LPE in several solvents (see Methods for details). LPE takes advantage of ultrasonic cavitation in liquids such as water or organic solvents to break apart bulk crystals, and can be scaled up to produce a large quantity of nanosheets. Centrifugation immediately after sonication removes the bulky undispersed material while the dispersed nanosheet-rich supernatant is harvested. Fig. 3a shows a photo of B_4C dispersions in different organic solvents, which all appear very dark in colour, indicating high concentrations of B_4C. The dispersions all remained stable with no visible precipitation even after several months. Out of all the solvents used, B_4C sonicated in isopropyl alcohol (IPA) generated the least amount of residue when deposited onto substrates for characterization. Some further results regarding the stability of the B_4C nanosheets are shown in the ESI (Fig. S6†). We note that several different organic solvents produced good dispersions of B_4C here, but are not necessarily suitable for LPE of conventional vdW 2D materials due to differences in the cleavage and dispersion mechanisms, which may involve differences in surface energies, solvent polarity and viscosity, bond breaking, surface reconstruction, *etc*.

Fig. 3b shows a TEM image of the B_4C nanosheet with dimensions of approximately 250 nm × 100 nm. Fig. 3c and d shows a B_4C nanosheet with a thickness of 5 nm on a SiO_2/Si substrate after spin coating (see Methods for details), with a lateral size of about 500 nm.

We analysed a total of 169 B_4C nanosheets in AFM images to produce histograms of their thickness and area (see Methods for details). Fig. 4a is an example of an AFM image showing several LPE-generated B_4C nanosheets deposited on a SiO_2/Si substrate and Fig. 4b shows the height profile for selected nanosheets in Fig. 4a along the dashed lines labelled 1–6. Fig. 4c shows the histogram of the thickness of B_4C flakes produced by analysing multiple images similar to Fig. 4a. We

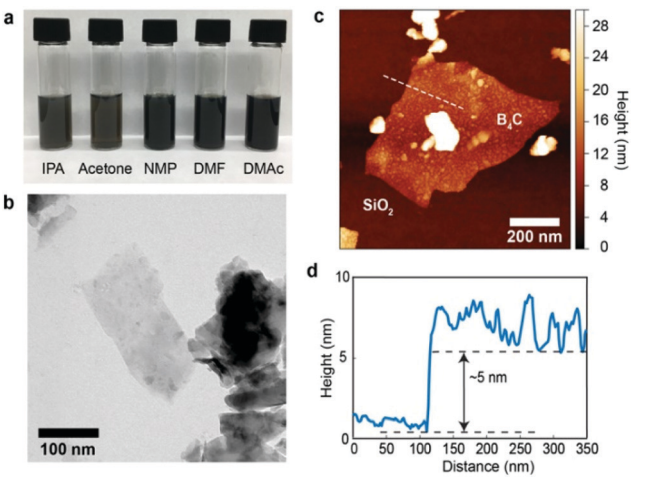

Fig. 3 Liquid-phase exfoliation (LPE) of B_4C nanosheets. (a) Vials of B_4C nanosheets in five different organic solvents: isopropanol (IPA), acetone, *N*-methyl-2-pyrrolidone (NMP), dimethylformamide (DMF) and dimethylacetamide (DMAc). (b) TEM image of B_4C nanosheets dispersed in IPA. (c) AFM image of B_4C nanosheet dispersed in IPA and deposited on SiO_2/Si substrate. (d) Height profile along the dashed line in (a) indicating the ~5 nm thickness of the nanosheet.

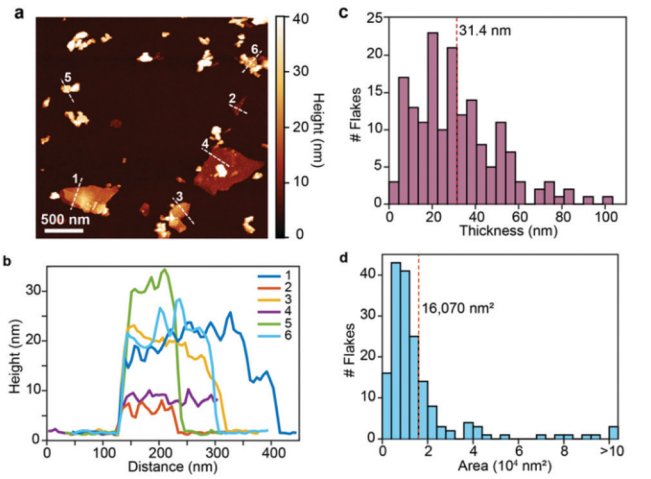

Fig. 4 Atomic force microscopy of B_4C nanoflakes from LPE. (a) Representative AFM image of LPE-produced B_4C flakes spin coated on Si/SiO_2 wafer. (b) Height profiles of six selected flakes in (a). (c) Histogram of thickness of B_4C nanosheets measured from AFM. The red dashed line indicates the mean thickness at 31.4 nm. (d) Histogram of area of B_4C nanosheets with the dashed red line indicating the mean nanosheet area at 16 070 nm^2.

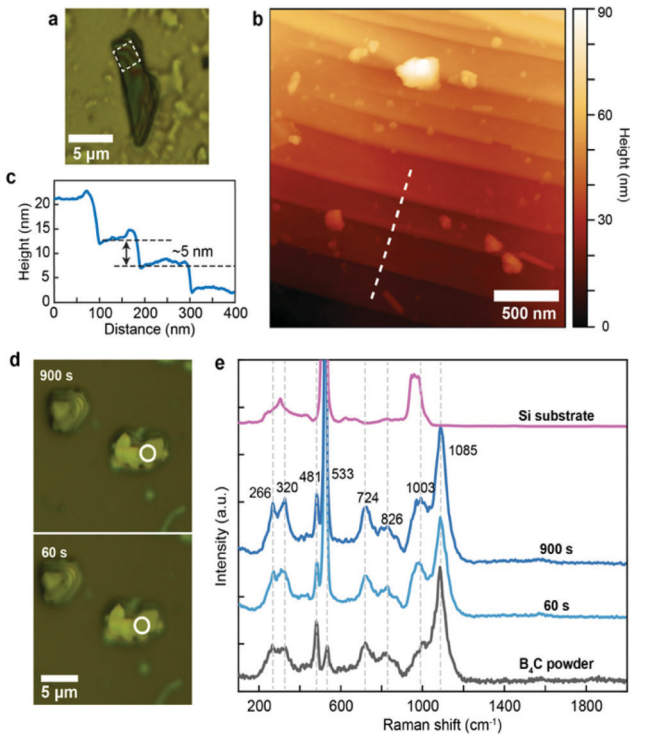

Fig. 5 Mechanically exfoliated B_4C nanosheets. (a) Optical microscopy image of mechanically exfoliated B_4C nanosheet deposited on a gold-coated SiO_2 substrate. (b) AFM image of step edges on the B_4C nanosheet in (a) in the area marked by the white square. (c) Height profile along the dashed line in (b) showing ~5 nm steps. (d) Optical images of mechanically exfoliated B_4C flake on SiO_2/Si substrate after 60 s and 900 s laser exposure (the location where the laser is hitting is marked by the circle). (e) Raman spectra for untreated bulk B_4C powder and the same B_4C flake from panel (d) after 60 s and 900 s laser exposure time, and the bare Si substrate. Prominent peaks from the B_4C spectrum at the labelled wavenumber positions.

find that the flakes are between 4 to 106 nm thick, with the majority of the flakes found between 4 and 60 nm, with a mean thickness of 31.4 nm. Fig. 4d shows the histogram of the area of B_4C flakes. The mean value for the area is 16 070 nm^2, which correlates to approximate dimensions of ~150 nm × 100 nm for typical flakes.

Mechanically exfoliated B_4C

After the formation of B_4C nanosheets *via* LPE, mechanical exfoliation (ME) was performed on bulk B_4C powder (see Methods for details) in order to obtain samples from a less disruptive method to conduct further characterization. Because B_4C has much stronger bonding between atoms and is not a van der Waals material, the resulting flakes were usually a few hundreds of nanometres thick with a lateral size of a few micrometres across. From our experiments, we found that gold-coated Si/SiO_2 substrates resulted in better adhesion to the B_4C than Si/SiO_2 alone. Fig. 5a shows an optical microscope image of a thick ME B_4C flake on a gold-coated SiO_2/Si substrate. Although the ME B_4C flakes are rather thick compared to LPE B_4C flakes, the AFM image in Fig. 5b shows flat step edges on the top of the ME B_4C flake in Fig. 5a, and provides some insight on the structure and cleavage into layers. Fig. 5c shows the height profile for the dashed line in Fig. 5b, showing that the height for each step edge is about 5 nm, which is similar to the thinnest B_4C nanosheets obtained from LPE (Fig. 3c). While ME in this case of a non-vdW material cannot produce nanometer-thick flakes, it does provide important confirmation of the cleavage at the surface.

Raman spectroscopy was performed on the mechanically exfoliated B_4C flakes. Fig. 5d shows the optical images of the characterized flake after 60 s and 900 s of laser exposure (see Methods for details). The flake remained intact and no obvious change was seen for the Raman spectra as plotted in Fig. 5e. There is some debate about the true nature of the two peaks at 266 and 320 cm^{-1}, but according to Werheit *et al.*, they likely originate from the rotation of C–B–C and C–B–B chains (when carbon content in the B_4C is low) associated with the wagging modes of the icosahedra, and tend to decrease in intensity with decreasing carbon content.[19,68–72] Both the 481 and 533 cm^{-1} peaks are linked to the stretching vibrations of the C–B–C chains.[19,73] The peak at 481 cm^{-1} is believed to be the chain rotation perpendicular to the (111) plane, which was first suggested by calculations by Lazzari *et al.*[29] It was then experimentally confirmed by Domnich *et al.* using B_4C with different orientations. They found the intensity of the 481 cm^{-1} peak decreased when the sample was rotated to different angles from the (111) orientation.[19] This was also confirmed by Vatst *et al.*, since the atomic displacement was the greatest when the C–B–C chain is at 90° to the chain axis.[29] We note that in the Raman spectrum in Fig. 5e, the 533 cm^{-1} peak is very close to the SiO_2 bulk peak at 520 cm^{-1} and can be difficult to resolve. The vibrations within the icosahedral

units are commonly believed to be the source for the peaks between 600 to 1200 cm^{-1}.[29,73] The prominent peak at 1088 cm^{-1} is a high stiffness vibration mode in B_4C that was shown by Domnich *et al.* to have no pressure dependence.[19] These main Raman peaks for B_4C are observed in the bulk powder material, mechanically exfoliated, and liquid phase exfoliated nanosheets.

Evolution of Raman spectra of LPE-produced B_4C nanosheets

The Raman spectra of 50 individual B_4C nanosheets produced by LPE were analysed as a function of laser irradiation time. We identified four general types of flakes depending on how their Raman spectra evolve with increasing laser irradiation time. Changes in the relative intensities of Raman peaks associated with the B_4C crystal and peaks associated with carbon-rich phases were observed, as shown in Fig. 6. In contrast, the ME B_4C flakes had consistent Raman spectra that did not change with laser irradiation time.

Representative spectra from the four types of flakes of LPE B_4C are plotted in Fig. 6, which are labelled Type I to Type IV in panels (a) to (d), with the percentage of flakes exhibiting each type of behaviour given in the parentheses. In panel (a), all the main B_4C characteristic peaks are labelled from 266 to 1083 cm^{-1}. Peaks coming from graphitic or carbonaceous phases, the D band (~1350 cm^{-1}) and G band (1590 cm^{-1}), are also labelled. Previous work on the mechanical deformation of B_4C has shown the formation of carbon-rich amorphous regions that contribute these peaks.[74–78] Also, small peaks from the sapphire substrate are labelled with asterisks. Representative plots of the evolution of the ratio of intensities of the D band to the B_4C peak at 1080 cm^{-1} as a function of laser irradiation time are shown in Fig. 6e. That is, this ratio represents the amount of carbon-rich amorphous regions compared to the amount of B_4C.

Type I is the most frequently seen, corresponding to about 64% of the total flakes that were analysed (Fig. 6a). In this type, the spectrum starts with small peaks associated with a carbon-rich phase, and all the other characteristic B_4C peaks, but the carbon peaks disappear after a short laser exposure time. The intensities of all the B_4C peaks also decrease steadily with prolonged laser exposure. The sapphire peak labelled with the asterisk can be seen in the last stage as the flake becomes thinner and thinner with increasing laser irradiation time. We speculate that this behaviour may be because the B_4C flakes were coated by a thin layer of amorphous carbon generated during the LPE exfoliation, which could then be easily removed by the laser to reveal the relatively undamaged B_4C beneath.

The main difference between Type II and Type I is the initial intensity of the carbon peaks: Type I flakes start with small carbon peaks, while Type II flakes start with strong carbon peaks. The B_4C peaks gradually become sharper while the carbon peaks decrease steadily with laser exposure and are gone by the last stage. It is noticeable that some flakes become thinner in the end such that the peak from the sapphire substrate (labelled with the asterisk at 420 cm^{-1}) becomes sharp

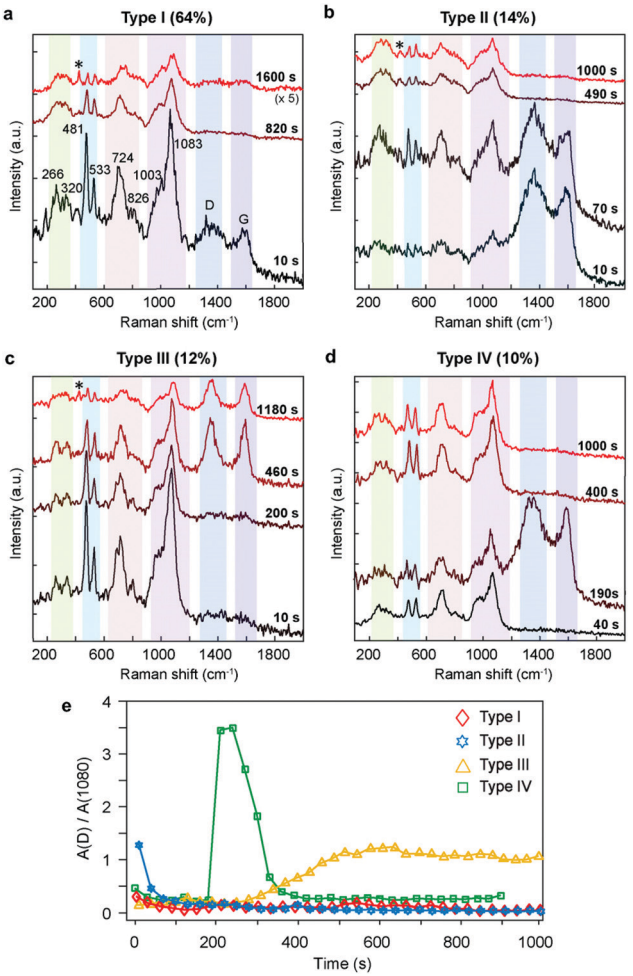

Fig. 6 Comparison of evolution of Raman spectra for LPE-produced B_4C flakes. Raman spectra were continuously acquired over several minutes from 50 individual B_4C flakes. Over time, the features in the Raman spectra evolved and were divided into four types. (a–d) Representative Raman spectra over time categorized as Types I to IV. The main peaks from B_4C are labelled with numbers indicating their wavenumber positions. The peak from the sapphire substrate is marked with *. (e) The ratio of the area of the D band peak at ~1350 cm^{-1} and the area of the prominent B_4C peak at 1080 cm^{-1} is plotted as a function of laser exposure time for four representative B_4C nanosheets, one from each type.

and prominent. Approximately 14% of the examined flakes showed this kind of Raman spectrum. It is also notable that the ratio of peak intensities between the 481 cm^{-1} and 533 cm^{-1} peaks varies from 2 : 1 to 1 : 1 (see Fig. S4†) for type I and type II, which could be attributed to the transition of the C–B–C chains to the C–B–B chains as carbon atoms were lost during the chain breaking process.[73]

Type III flakes (Fig. 6c) start with all the strong characteristic B_4C peaks but no noticeable carbon peaks, but then the D and G bands appear in the middle stage (between 350 s to 750 s of irradiation) and remain present. Approximately 12% of the flakes showed this behaviour. Type IV (Fig. 6d) starts without carbon peaks, but they soon show up (typically

between 200 s to 400 s). Then, the intensity of the carbon peaks diminishes drastically and disappear in the final stage. Approximately 10% of flakes showed this behaviour. Representative time traces of all four types of behaviour are shown in Fig. 6e (see Fig. S5† for additional time traces).

Based on these Raman spectra, it is likely that graphitic domains are formed on the surfaces of and even inside the cleaved B_4C as a result of exfoliation. In graphitic domains, the peak at ~1300–1360 cm^{-1} can be ascribed to the breathing vibrations of the aromatic rings and is normally attributed to disorder in the carbon bonding and is called the D band, while the peak at ~1580–1590 cm^{-1} can be ascribed to the in-plane vibration of the sp^2 C=C bond and is known as the G band.[79,80] We believe that the formation and the evolution of these carbon peaks could be a combined effect of the different planes within the B_4C structure that are cleaved, the defects induced by the mechanical forces applied during LPE, and the damage from the laser power with increasing irradiation time. These effects are described in more detail below.[73–78]

The plane of cleavage or exfoliation within the B_4C crystal controls the arrangement of atoms on the surface of each flake, and so some surfaces may have more carbon atoms exposed to the laser as described in the computational results section and in the (ESI†). Tallant *et al.* showed how the C–B–C chains change into C–B–B chains when the carbon content was decreased; the "freed" carbon atoms can then form graphitic carbon and contribute to the formation of the D and G bands.[73] The degree of defects in the re-formed carbon regions affects the D band intensity. As mentioned earlier, the 481 cm^{-1} peak in the B_4C spectrum originates from the chain rotation perpendicular to the (111) plane. Thus, different cleavage planes are expected to have a major effect on the Raman spectrum due to the nature of the C–B–C chains and icosahedra in the B_4C structure: different planes have very different vibrational and rotational modes and the atomic displacement also varies from different angles between the chains and the icosahedra.[25] Furthermore, in relatively thin nanosheets rather than the bulk, the effect of surface features will tend to dominate the measured spectra.

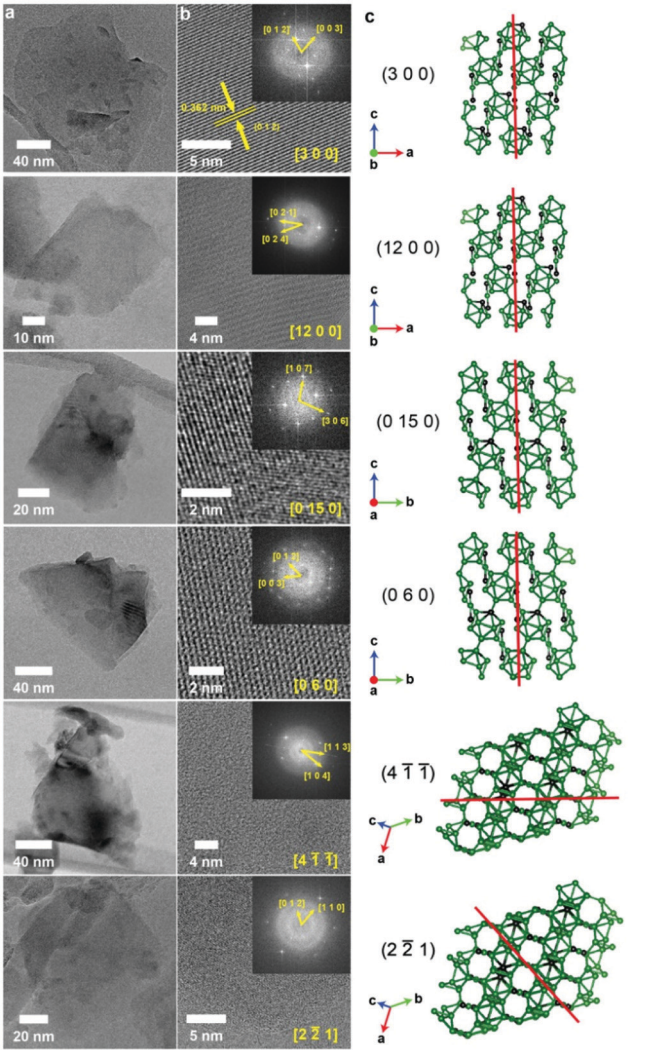

Fig. 7 (a) HRTEM images showing the morphology of selected flakes. (b) Zoomed in images of flakes from (a) with inset showing FFTs annotated with vectors used to determine exfoliation plane. (c) Crystal structures for B_4C showing the calculated exfoliation planes in the HRTEM data shown in (a) and (b).

HRTEM of LPE-produced B_4C and cleavage plane analysis

High-resolution transmission electron microscopy (HRTEM) was used to image the LPE-produced B_4C nanosheets to further study their morphology and crystal structure, and to find evidence of different cleavage planes as suggested by the DFT results. Representative HRTEM images of LPE B_4C nanosheets are shown in Fig. 7 column a, showing sheet-like structures. Zoomed in images of the same flakes are shown in Fig. 7 column b, depicting various crystallographic orientations. The insets in column b feature the fast Fourier transforms (FFTs) of the HRTEM images. The lattice spacing in one image is indicated in the first image of column b. As described in the Methods section above, the cleavage planes are calculated using the cross product of two vectors indexed in a given FFT pattern. Arrows depicting the vectors chosen for the cross-product calculation for the flakes shown in Fig. 7 are shown in the inset FFTs.

We have examined over 30 flakes by HRTEM, and based on our analysis have found many different possible cleavage planes exhibited by exfoliated B_4C nanosheets. One such observed cleavage plane, the (300) plane depicted in the first row of Fig. 7, is one of the planes we have extensively examined through computational modelling above. While we have seen the presence of the (300) plane and other planes from the {100} family we have observed no instance of any of the other planes we have modelled above. However, we do note the similarities between the {100} and {010} families of planes, as depicted along with the calculated cleavage planes of the other flakes in Fig. 7 in column c. It is worth mentioning that these two families are among two of the more common planes we

have observed across all of the flakes we have analysed, and are consistent with the planes with the lower formation energies from the earlier computational analysis (see Fig. 2). However, there are indeed many possible cleavage planes that we have experimentally observed, also in agreement with the computational results that many planes are energetically favourable and can result in stable nanosheets.

However, we also observe experimental evidence of planes that do not bear many similarities to flakes we have examined in our computational analysis, depicted in the last two rows of Fig. 7: the $(4\bar{1}\bar{1})$ and $(2\bar{2}1)$ planes. As seen in the diagram of the crystal structures in Fig. 7, column c, exfoliation along the final two cleavage planes results in some combination of breakage of the icosahedra and breakage of the C–B–C chains. The observation of multiple possible exfoliation planes with different resulting bond breaking events suggests the behaviour of B_4C upon exfoliation in solution-phase is more complex than what is observed in anisotropic or layered materials. These observations are also consistent with our computational results, which showed that the different cleavage planes did not show a significant difference in formation energies, indicating that many planes are similarly energetically favourable for cleavage.

Conclusions

In conclusion, we have produced boron carbide nanosheets with nanometre-scale thickness for the first time by liquid exfoliation of boron carbide bulk power in several solvents. Histograms of AFM images show the average thickness and surface area for the B_4C nanosheets are 31.4 nm and 16 070 nm^2, respectively. The thinnest B_4C flake we found was approximately 5 nm thick, about the same height of the step edges we found on the top surface of a mechanically exfoliated B_4C flake. Our DFT calculations showed the formation energies of four possible exfoliation planes (001), (101), (300) and (012) at different termination positions are below the threshold of 0.2 eV per atom for free-standing monolayer or few-layer nanosheets, indicating that it is energetically feasible to cleave B_4C along these planes, in many cases involving the breaking of boron icosahedra and formation of new boron cage structures. The similar formation energies for cleavage along different planes suggests that there are multiple ways to cleave the B_4C structure to form nanosheets. We found experimental evidence *via* HRTEM imaging of the exfoliation of B_4C along the (300) plane and other planes within the {100} family in addition to the structurally equivalent {010} family. We also note experimental evidence for many other planes including $(4\bar{1}\bar{1})$ and $(2\bar{2}1)$ planes, suggesting the rich exfoliation behaviour of B_4C in the liquid-phase exfoliation process. The cleavage along a variety of planes in B_4C is also reflected in the different behaviours observed by Raman spectroscopy, where peaks from the B_4C structure and from carbon-rich amorphous regions are observed to change with laser irradiation time. We anticipate the successful exfoliation of B_4C nanosheets will pave the way for future applications in areas such as catalysts, mechanical strengthening and batteries or fuel cells.

Conflicts of interest

There are no conflicts to declare.

Acknowledgements

We gratefully acknowledge the use of facilities within the Eyring Materials Center at Arizona State University. We also thank Prof. H. Yan for use of his AFM and Raman system and Dr Shuoxing Jiang for assistance with AFM measurements. AAG, QHW, YG, and MSG were supported by NSF grant DMR-1610153. QHW, AS, YG, and AG were supported by NSF grant DMR-1906030. AS acknowledges computational resources awarded by the NSF-XSEDE, under Award No. TGDMR150006, and the ASU research computing centre.

References

1 J. N. Coleman, M. Lotya, A. O'Neill, S. D. Bergin, P. J. King, U. Khan, K. Young, A. Gaucher, S. De, R. J. Smith, I. V. Shvets, S. K. Arora, G. Stanton, H.-Y. Kim, K. Lee, G. T. Kim, G. S. Duesberg, T. Hallam, J. J. Boland, J. J. Wang, J. F. Donegan, J. C. Grunlan, G. Moriarty, A. Shmeliov, R. J. Nicholls, J. M. Perkins, E. M. Grieveson, K. Theuwissen, D. W. McComb, P. D. Nellist and V. Nicolosi, *Science*, 2011, **331**, 568–571.
2 V. Nicolosi, M. Chhowalla, M. G. Kanatzidis, M. S. Strano and J. N. Coleman, *Science*, 2013, **340**, 1226419.
3 L. Niu, J. N. Coleman, H. Zhang, H. Shin, M. Chhowalla and Z. Zheng, *Small*, 2016, **12**, 272–293.
4 F. Bonaccorso, A. Bartolotta, J. N. Coleman and C. Backes, *Adv. Mater.*, 2016, **28**, 6136–6166.
5 T. Sasaki, F. Kooli, M. Iida, Y. Michiue, S. Takenouchi, Y. Yajima, F. Izumi, B. C. Chakoumakos and M. Watanabe, *Chem. Mater.*, 1998, **10**, 4123–4128.
6 Z. Liu, K. Ooi, H. Kanoh, W. Tang and T. Tomida, *Langmuir*, 2000, **16**, 4154–4164.
7 R. J. Smith, P. J. King, M. Lotya, C. Wirtz, U. Khan, S. De, A. O'Neill, G. S. Duesberg, J. C. Grunlan, G. Moriarty, J. Chen, J. Wang, A. I. Minett, V. Nicolosi and J. N. Coleman, *Adv. Mater.*, 2011, **23**, 3944–3948.
8 G. Cunningham, M. Lotya, C. S. Cucinotta, S. Sanvito, S. D. Bergin, R. Menzel, M. S. P. Shaffer and J. N. Coleman, *ACS Nano*, 2012, **6**, 3468–3480.
9 S. K. Das and K. Jasuja, *ACS Appl. Nano Mater.*, 2018, **1**, 1612–1622.
10 A. Yousaf, M. S. Gilliam, S. L. Y. Chang, M. Augustin, Y. Guo, F. Tahir, M. Wang, A. Schwindt, X. S. Chu, D. O. Li, S. Kale, A. Debnath, Y. Liu, M. D. Green, E. J. G. Santos, A. A. Green and Q. H. Wang, arXiv:cond-mat/2001.09237.

11 A. Puthirath Balan, S. Radhakrishnan, C. F. Woellner, S. K. Sinha, L. Deng, C. de los Reyes, B. M. Rao, M. Paulose, R. Neupane, A. Apte, V. Kochat, R. Vajtai, A. R. Harutyunyan, C.-W. Chu, G. Costin, D. S. Galvao, A. A. Martí, P. A. van Aken, O. K. Varghese, C. S. Tiwary, A. M. M. R. Iyer and P. M. Ajayan, *Nat. Nanotechnol.*, 2018, **13**, 602–609.

12 A. Puthirath Balan, S. Radhakrishnan, R. Kumar, R. Neupane, S. K. Sinha, L. Deng, C. A. de los Reyes, A. Apte, B. M. Rao, M. Paulose, R. Vajtai, C. W. Chu, G. Costin, A. A. Martí, O. K. Varghese, A. K. Singh, C. S. Tiwary, M. R. Anantharaman and P. M. Ajayan, *Chem. Mater.*, 2018, **30**, 5923–5931.

13 C. Backes, D. Campi, B. M. Szydlowska, K. Synnatschke, E. Ojala, F. Rashvand, A. Harvey, A. Griffin, Z. Sofer, N. Marzari, J. N. Coleman and D. D. O'Regan, *ACS Nano*, 2019, **13**, 7050–7061.

14 H. Kaur, R. Tian, A. Roy, M. McCrystall, D. V. Horvath, A. M. M. R. Iyer, R. Smith, M. Ruether, A. Griffin, C. Backes, V. Nicolosi and J. N. Coleman, *ACS Nano*, 2020, **14**, 13418–13432.

15 C. Backes, R. J. Smith, N. McEvoy, N. C. Berner, D. McCloskey, H. C. Nerl, A. O'Neill, P. J. King, T. Higgins, D. Hanlon, N. Scheuschner, J. Maultzsch, L. Houben, G. S. Duesberg, J. F. Donegan, V. Nicolosi and J. N. Coleman, *Nat. Commun.*, 2014, **5**, 4576.

16 G. Guan, J. Xia, S. Liu, Y. Cheng, S. Bai, S. Y. Tee, Y.-W. Zhang and M.-Y. Han, *Adv. Mater.*, 2017, **29**, 1700326.

17 C. Xing, Z. Xie, Z. Liang, W. Liang, T. Fan, J. S. Ponraj, S. C. Dhanabalan, D. Fan and H. Zhang, *Adv. Opt. Mater.*, 2017, **5**, 1700884.

18 Z. Xie, C. Xing, W. Huang, T. Fan, Z. Li, J. Zhao, Y. Xiang, Z. Guo, J. Li, Z. Yang, B. Dong, J. Qu, D. Fan and H. Zhang, *Adv. Funct. Mater.*, 2018, **28**, 1705833.

19 V. Domnich, S. Reynaud, R. A. Haber and M. Chhowalla, *J. Am. Ceram. Soc.*, 2011, **94**, 3605–3628.

20 S. Mondal, E. Bykova, S. Dey, S. I. Ali, N. Dubrovinskaia, L. Dubrovinsky, G. Parakhonskiy and S. van Smaalen, *Sci. Rep.*, 2016, **6**, 19330.

21 G. Fanchini, J. W. McCauley and M. Chhowalla, *Phys. Rev. Lett.*, 2006, **97**, 035502.

22 K. Rasim, R. Ramlau, A. Leithe-Jasper, T. Mori, U. Burkhardt, H. Borrmann, W. Schnelle, C. Carbogno, M. Scheffler and Y. Grin, *Angew. Chem.*, 2018, **130**, 6238–6243.

23 H. K. Clark and J. L. Hoard, *J. Am. Chem. Soc.*, 1943, **65**, 2115–2119.

24 V. I. Ivashchenko, V. I. Shevchenko and P. E. A. Turchi, *Phys. Rev. B*, 2009, **80**, 235208.

25 R. Lazzari, N. Vast, J. M. Besson, S. Baroni and A. Dal Corso, *Phys. Rev. Lett.*, 1999, **83**, 3230–3233.

26 S. Lee, D. M. Bylander and L. Kleinman, *Phys. Rev. B*, 1992, **45**, 3245–3247.

27 N. Vast, J. Sjakste and E. Betranhandy, *J. Phys.: Conf. Ser.*, 2009, **176**, 012002.

28 D. Emin, *Phys. Rev. B*, 1988, **38**, 6041–6055.

29 N. Vast, R. Lazzari, J. M. Besson, S. Baroni and A. Dal Corso, *Comput. Mater. Sci.*, 2000, **17**, 127–132.

30 S. Aydin and M. Simsek, *Phys. Status Solidi B*, 2009, **246**, 62–70.

31 K. Shirai, *J. Superhard Mater.*, 2010, **32**, 205–225.

32 S. Mu, X. Chen, R. Sun, X. Liu, H. Wu, D. He and K. Cheng, *Carbon*, 2016, **103**, 449–456.

33 S. Song, W. Xu, R. Cao, L. Luo, M. H. Engelhard, M. E. Bowden, B. Liu, L. Estevez, C.-M. Wang and J.-G. Zhang, *Nano Energy*, 2017, **33**, 195–204.

34 E. Antolini and E. R. Gonzalez, *Solid State Ionics*, 2009, **180**, 746–763.

35 M. Minakshi and M. G. Blackford, *Mater. Chem. Phys.*, 2010, **123**, 700–705.

36 J. Kim, B.-C. Lee, Y. R. Uhm and W. H. Miller, *J. Nucl. Mater.*, 2014, **453**, 48–53.

37 M. A. Kiani, S. J. Ahmadi, M. Outokesh, R. Adeli and A. Mohammadi, *Radiat. Phys. Chem.*, 2017, **141**, 223–228.

38 X. Li, J. Wu, C. Tang, Z. He, P. Yuan, Y. Sun, W. Lau, K. Zhang, J. Mei and Y. Huang, *Composites, Part B*, 2019, **159**, 355–361.

39 M. Alizadeh, M. Alizadeh and R. Amini, *J. Mater. Sci. Technol.*, 2013, **29**, 725–730.

40 J. Du, Q. Li, Y. Xia, X. Cheng, Y. Gan, H. Huang, W. Zhang and X. Tao, *J. Alloys Compd.*, 2013, **581**, 128–132.

41 X. Tao, L. Dong, X. Wang, W. Zhang, B. J. Nelson and X. Li, *Adv. Mater.*, 2010, **22**, 2055–2059.

42 R. Ma and Y. Bando, *Chem. Mater.*, 2002, **14**, 4403–4407.

43 M. J. Pender, K. M. Forsthoefel and L. G. Sneddon, *Pure Appl. Chem.*, 2003, **75**, 1287–1294.

44 Y. Ishikawa, Y. Shimizu, T. Sasaki and N. Koshizaki, *Appl. Phys. Lett.*, 2007, **91**, 161110.

45 M. W. Mortensen, O. Björkdahl, P. G. Sørensen, T. Hansen, M. R. Jensen, H. J. G. Gundersen and T. Bjørnholm, *Bioconjugate Chem.*, 2006, **17**, 284–290.

46 Z. Guan, T. Gutu, J. Yang, Y. Yang, A. A. Zinn, D. Li and T. T. Xu, *J. Mater. Chem.*, 2012, **22**, 9853–9860.

47 Y. Liu, Q. Tian, S. Wang, Z. Li, X. Duan, L. Que and C. Pei, *Ceram. Int.*, 2020, **46**, 18131–18141.

48 H. H. Nersisyan, B. U. Yoo, S. H. Joo, T. H. Lee, K.-H. Lee and J.-H. Lee, *Chem. Eng. J.*, 2015, **281**, 218–226.

49 F.-F. Xu and Y. Bando, *J. Phys. Chem. B*, 2004, **108**, 7651–7655.

50 W.-B. Qiu, Y.-X. Luo, R.-P. Liang, J.-D. Qiu and X.-H. Xia, *Chem. Commun.*, 2019, **55**, 7406–7409.

51 W. Qiu, X.-Y. Xie, J. Qiu, W.-H. Fang, R. Liang, X. Ren, X. Ji, G. Cui, A. M. Asiri, G. Cui, B. Tang and X. Sun, *Nat. Commun.*, 2018, **9**, 3485.

52 S. Haastrup, M. Strange, M. Pandey, T. Deilmann, P. S. Schmidt, N. F. Hinsche, M. N. Gjerding, D. Torelli, P. M. Larsen, A. C. Riis-Jensen, J. Gath, K. W. Jacobsen, J. J. Mortensen, T. Olsen and K. S. Thygesen, *2D Mater.*, 2018, **5**, 042002.

53 A. K. Singh, K. Mathew, H. L. Zhuang and R. G. Hennig, *J. Phys. Chem. Lett.*, 2015, **6**, 1087–1098.

54 G. Kresse and J. Furthmüller, *Comput. Mater. Sci.*, 1996, **6**, 15–50.

55 G. Kresse and J. Furthmüller, *Phys. Rev. B*, 1996, **54**, 11169–11186.
56 G. Kresse and J. Hafner, *Phys. Rev. B*, 1994, **49**, 14251–14269.
57 G. Kresse and J. Hafner, *Phys. Rev. B*, 1993, **48**, 13115–13118.
58 G. Román-Pérez and J. M. Soler, *Phys. Rev. Lett.*, 2009, **103**, 096102.
59 M. Dion, H. Rydberg, E. Schröder, D. C. Langreth and B. I. Lundqvist, *Phys. Rev. Lett.*, 2005, **95**, 109902.
60 J. Klimeš, D. R. Bowler and A. Michaelides, *Phys. Rev. B*, 2011, **83**, 195131.
61 S. P. Ong, W. D. Richards, A. Jain, G. Hautier, M. Kocher, S. Cholia, D. Gunter, V. Chevrier, K. A. Persson and G. Ceder, *Comput. Mater. Sci.*, 2013, **68**, 314–319.
62 A. Jain, S. P. Ong, G. Hautier, W. Chen, W. D. Richards, S. Dacek, S. Cholia, D. Gunter, D. Skinner, G. Ceder and K. A. Persson, *APL Mater.*, 2013, **1**, 011002.
63 D. Nečas and P. Klapetek, *Open Phys.*, 2011, **10**, 181–188.
64 D. Emin, *Phys. Today*, 2008, **40**, 55.
65 K. Y. Xie, Q. An, T. Sato, A. J. Breen, S. P. Ringer, W. A. Goddard, J. M. Cairney and K. J. Hemker, *Proc. Natl. Acad. Sci. U. S. A.*, 2016, **113**, 12012–12016.
66 D. Emin, *J. Solid State Chem.*, 2006, **179**, 2791–2798.
67 G. Henkelman, A. Arnaldsson and H. Jónsson, *Comput. Mater. Sci.*, 2006, **36**, 354–360.
68 U. Kuhlmann and H. Werheit, *Phys. Status Solidi B*, 1993, **175**, 85–92.
69 H. Werheit, R. Schmechel, U. Kuhlmann, T. U. Kampen, W. Mönch and A. Rau, *J. Alloys Compd.*, 1999, **291**, 28–32.
70 H. Werheit, H. W. Rotter, F. D. Meyer, H. Hillebrecht, S. O. Shalamberidze, T. G. Abzianidze and G. G. Esadze, *J. Solid State Chem.*, 2004, **177**, 569–574.
71 U. Kuhlmann and H. Werheit, *J. Alloys Compd.*, 1994, **205**, 87–91.
72 S.-W. Oh, J. W. E. Weiss, P. A. Kerneghan, I. Korobkov, K. E. Maly and D. L. Bryce, *Magn. Reson. Chem.*, 2012, **50**, 388–401.
73 D. R. Tallant, T. L. Aselage, A. N. Campbell and D. Emin, *Phys. Rev. B*, 1989, **40**, 5649–5656.
74 V. Domnich, Y. Gogotsi, M. Trenary and T. Tanaka, *Appl. Phys. Lett.*, 2002, **81**, 3783–3785.
75 X. Q. Yan, W. J. Li, T. Goto and M. W. Chen, *Appl. Phys. Lett.*, 2006, **88**, 131905.
76 D. Ghosh, G. Subhash, C. H. Lee and Y. K. Yap, *Appl. Phys. Lett.*, 2007, **91**, 061910.
77 M. Chen and J. W. McCauley, *J. Appl. Phys.*, 2006, **100**, 123517.
78 D. Ge, V. Domnich, T. Juliano, E. A. Stach and Y. Gogotsi, *Acta Mater.*, 2004, **52**, 3921–3927.
79 L. Escobar-Alarcón, M. E. Espinosa-Pesqueira, D. A. Solis-Casados, J. Gonzalo, J. Solis, M. Martinez-Orts and E. Haro-Poniatowski, *Appl. Phys. A*, 2018, **124**, 141.
80 M. J. Matthews, M. A. Pimenta, G. Dresselhaus, M. S. Dresselhaus and M. Endo, *Phys. Rev. B: Condens. Matter Mater. Phys.*, 1999, **59**, R6585–R6588.

